Metal Ions in the Atmosphere of Neptune

James R. Lyons

Microwave propagation experiments performed with Voyager 2 at Neptune revealed sharp layers of electrons in Neptune's lower ionosphere with densities of ~10^4 per cubic centimeter. These layers are reminiscent of the sporadic-E layers in the Earth's ionosphere, and when taken together with data from the other giant planets, these data confirm the importance of the magnetic field in layer formation. A photochemical model that incorporates species produced by meteoroid ablation predicts that singly ionized magnesium is the most likely metal to be found in the layers, although laboratory data on the kinetics of metallic atoms and ions in a reducing environment are lacking. The metal chemistry discussed here is directly relevant to the abundant metals observed at the impact site of the G fragment of comet Shoemaker Levy 9 on Jupiter.

With the completion of the planetary component of the Voyager mission (*1*), we now have spacecraft data for nine ionospheres in the solar system. These data, together with the wealth of information on Earth's ionosphere, provide an excellent opportunity for comparative planetology. Seven of the ionospheres studied are in the outer solar system (Jupiter, Io, Saturn, Titan, Uranus, Neptune, and Triton) and have been investigated with the radio occultation technique pioneered by Lindal and colleagues (*2*). The ionospheres of Venus and Mars have been probed by both the radio occultation technique and in situ plasma instruments (*3*). Earth's ionosphere has been studied in great detail by in situ and ground-based radar techniques (*4*) but has not yet been probed in detail by radio occultations (*5*). I focus here on the lower ionosphere of Neptune, although much of the chemistry should be applicable to the upper atmospheres of the giant planets in general. Each of the giant planets exhibits sharp, high-density layers of electrons in its lower ionosphere (*6*). The absence of such layers in the ionospheres of the nonmagnetic planets demonstrates the key role played by the magnetic field in layer formation. On Earth, these layers consist primarily of metallic ions, produced during meteoroid ablation and gathered together by wind shears in the presence of Earth's magnetic field (*4*). Substantial modeling of terrestrial sporadic-E layers has been performed (*4*), but for the giant planets, only the influx of material from Io to Jupiter has been studied (*7*).

The radio occultation experiment at Neptune (*8*) was performed as Voyager 2 passed behind the planet as seen from Earth. Propagation effects along tangents through Neptune's atmosphere induced variations in the phases of the S-band (2.3 GHz) and X-band (8.4 GHz) spacecraft carriers. For a frequency $\omega \gg \omega_p$, the plasma frequency, the change in phase relative to a vacuum is given by (*9*)

$$\Delta\phi = -\frac{e^2}{2\epsilon_0 m_e \lambda \omega^2}\int_{\text{path}} N_e ds \qquad (1)$$

where e is the electron charge, m_e is the electron mass, ϵ_0 is the permittivity of free space, λ is the wavelength, and N_e is the electron number density. Contributions to $\Delta\phi$ come from all plasma along the ray path S, including the solar wind and the terrestrial ionosphere, but principally from Neptune's ionosphere. Figure 1 shows the S-band $\Delta\phi$ (versus time) measured during egress occultation when Voyager 2 was about 76,000 km behind the limb of Neptune. The integration time for each phase point is 0.1024 s, which, for a spacecraft velocity perpendicular to Neptune's limb of 12.8 km s^{-1}, corresponds to a vertical resolution of ~1.3 km. The diameter of the Fresnel zone, which characterizes the scale below which diffraction effects become important, is 6.3 km at S band and 3.3 km at X band for egress. The sharpest layers are 7 to 10 km in width and are therefore well sampled and not expected to produce significant diffraction, particularly at X band.

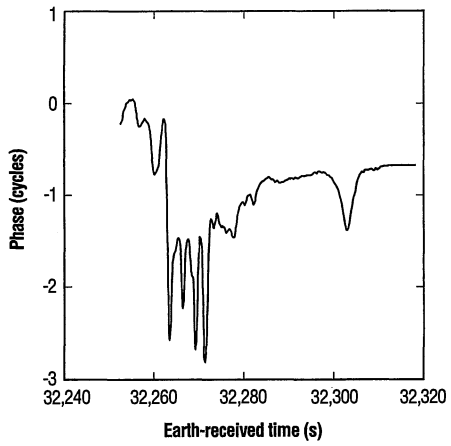

Fig. 1. Observed S-band phase perturbation due to passage of the spacecraft signal through Neptune's ionosphere at the egress occultation point. The phase, in cycles, is plotted against Earth-received time in seconds past midnight. One can convert the time scale to a distance scale by multiplying by the spacecraft velocity (perpendicular to the limb) of 12.8 km s^{-1}. There are four sharp layers between 32,260 and 32,280 s past midnight.

Assuming local spheroidal symmetry in the horizontal distribution of electrons, Lindal (*10*) inverted the phase data, obtaining N_e profiles for the ingress and egress locations. Figure 2 shows an expanded view of the lower ionosphere for egress; ingress data are shown in (*10*). The narrow structures in the phase (Fig. 1) correspond to the sharp layers seen in N_e at altitudes from ~650 to 750 km in Fig. 2. The high noise level of N_e in the layer region is most likely caused by deviations from local spheroidal symmetry (*10*, *11*). The net result is that the N_e values of the four main layers are uncertain by as much as a factor of 2, but the altitude of the layers is well determined. Another potential source of error, multipath propagation, can be shown to be unimportant everywhere in the ionosphere (*12*).

The simplest assumption regarding the origin of the layers is that, by analogy with Earth, they consist of long-lived metallic ions caught in a horizontal wind with a vertical shear (see below). However, the terrestrial ionosphere has also revealed that a richness of plasma structures can exist, due both to particle precipitation and to plasma instabilities. The latitude and longitude of the Neptune egress occultation point is 44°S, 229°W, which according to the magnetic model of Connerney *et al.* (*13*) corresponds to a magnetic field magnitude of B = 0.65 G, an inclination (or dip) angle of I = 65°, and a declination angle of D = −65°. Because egress occurred near the auroral zone, particle precipitation

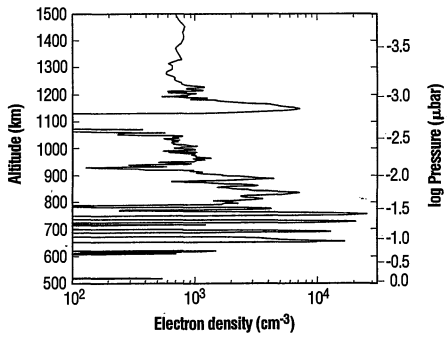

Fig. 2. Electron number density profile obtained (*10*) from inversion of the phase data in Fig. 1. The noise level above 1100 km is ~1000 cm^{-3}; below 1100 km, the noise level is significantly higher (~5000 to 10,000 cm^{-3}). Although the uncertainty in the electron abundance is high in the lower ionosphere, the altitude of the layers is well determined from the phase.

Division of Geological and Planetary Sciences, California Institute of Technology, Pasadena, CA 91125, USA.

must be considered. To form a layer at 700 km would require electrons with energy ~1 MeV, about 100 times the energy of terrestrial auroral electrons; protons are incapable of reaching such depths before undergoing charge exchange or ionizing the background gas. Plasma instabilities (*4*) may contribute to the observed structure, but given that the topside ion densities are only $\sim 1 \times 10^3$ cm^{-3}, instabilities probably are not responsible for the sharp layers in the lower ionosphere.

Another potential source of plasma structure is plasma drift across the terminator. Because of the distance to Neptune, the occultation points are necessarily both near the (morning) terminator; that is, the solar zenith angle is nearly 90°. Although diurnal variation due to radiative recombination of atomic ions is negligible, the low electron densities observed in the topside ionosphere suggest that a faster loss process may be occurring, so that plasma flow may be important.

To determine whether metallic ions could be responsible for the sharp layers observed in Neptune's lower ionosphere, I developed a comprehensive one-dimensional model of Neptune's upper atmosphere. The model extends from 1 to 10^{-10} mbar, accounts for eddy and molecular diffusion (*14*), and includes ion and neutral chemistry of hydrocarbons, water and related species, and "metals" (that is, species that do not contain C, H, O, or N). Metals are produced in the model by meteoroid ablation, with volume production rates as computed by Moses (*15*) for Neptune. The meteoroids are assumed to be of cometary composition (*16*), with 30% (by mass) water ice. The specific metal species considered are S, Si, Mg, Fe, and Na; in computing ablation production rates, no attempt was made to account for the differing volatilities of mineral grains that these species may occur in. The flux of meteoroids was taken to be 10 times the Oort cloud particle flux defined by Moses (*15*), which is roughly the geometric mean of the two fluxes considered in (*15*). Ablation was assumed to occur between 10 and 0.1 μbar, midway between the pure water ice and pure silicate ablation profiles of Moses (*15*). In the model, the eddy diffusion coefficient of Romani *et al.* (*17*) was used, with a CH_4 mixing ratio of 10^{-4} at 1 mbar.

Figure 3 shows the number density profiles predicted by the model for several neutral species, including four of the atomic metals. Neutral Si, although comparable to Fe and Mg in cosmic abundance, is rapidly consumed in reactions with C_2H_4 and other hydrocarbons and therefore does not accumulate in the atmosphere. The column production rate of Fe, Mg, and Si is 3.0×10^5 cm^{-2} s^{-1}, with peak production occurring from 425 to 500 km. Loss is primarily a result of recondensation onto dust particles (*18*), with a column rate of 2.7×10^5 cm^{-2} s^{-1} from 300 to 400 km. The condensation time scale in the model is $\sim 3 \times 10^5$ s at an altitude z of ~400 km, corresponding to a haze particle number density of ~300 cm^{-3} for 3-nm particles (*15*). At a rate about 1/10 that of condensation, loss of neutral metals also occurs by charge exchange with molecular ions.

There have been very few laboratory studies of the kinetics of the reactions of metal atoms with hydrocarbons. Defining M as one of Mg, Fe, Si, Na, or S, it is possible that species such as MH and MCH_3 are produced during reactions of M with larger hydrocarbons. It is likely that MH and MCH_3 will react with H to yield M and H_2 or CH_4, thus returning atomic metals to the system. Bond strengths have been measured for some metal hydrides (*19*), yielding values of ~2 eV, so that reactions with H and CH_3 would indeed be exothermic for the metals considered here. Except for Si and S, reactions of M with hydrocarbons are not included in the model. The model column densities of Mg and Fe are $\sim 6 \times 10^{11}$ cm^{-2}, and the column density of Na is $\sim 3 \times 10^{10}$ cm^{-2}. These column densities were not large enough to be detected by the Voyager spacecraft.

Ion profiles predicted by the model are shown in Fig. 4. The topside ionosphere is dominated by H^+. On the basis of recent measurements of the rate coefficient for dissociative recombination (*20*), H_3^+ is more than an order of magnitude less abundant than H^+. Water produced during meteoroid ablation reacts with H^+ to eventually produce H_3O^+ by a sequence of reactions described elsewhere (*6*, *21*). The model topside electron density is roughly five times the observed electron density (Fig. 2). There are several possible reasons for the discrepancy, which have been discussed elsewhere (*22*).

I predict that the lower ionosphere will be dominated by the metallic ions Mg^+ and Na^+ (Fig. 4). Metal ions are formed primarily by charge exchange with hydrocarbon ions and H_3O^+; solar ionization of neutral metals contributes <10% to the metal ion production rate in the model. The formation of hydrocarbon ions is driven by solar ionization of CH_4 and C_2 hydrocarbons and proceeds along a complex path (*6*, *23*) that leads to the formation of C_3 and C_4 hydrocarbon ions, here denoted as $C_3H_m^+$ and $C_4H_n^+$. The kinetics of hydrocarbon ion-molecule reactions have been well studied in the laboratory, and most rate coefficients are known (*24*). The principal formation pathway for metal ions is

$$C_3H_m^+ + M \rightarrow M^+ + C_3H_m \qquad (2)$$

The rate coefficient of this reaction is assumed to be 1×10^{-9} cm^3 s^{-1}, by analogy

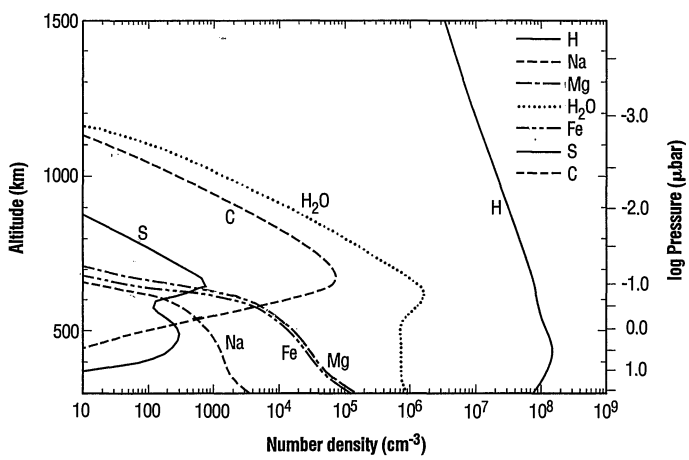

Fig. 3 (left). Model number density profiles for several "metal" species, water, C, and H. The calculations are for a meteoroid flux ~10 times the Oort cloud particle flux at Neptune (*15*). The meteoroid composition is assumed to be cometary with 30% water ice (by mass).

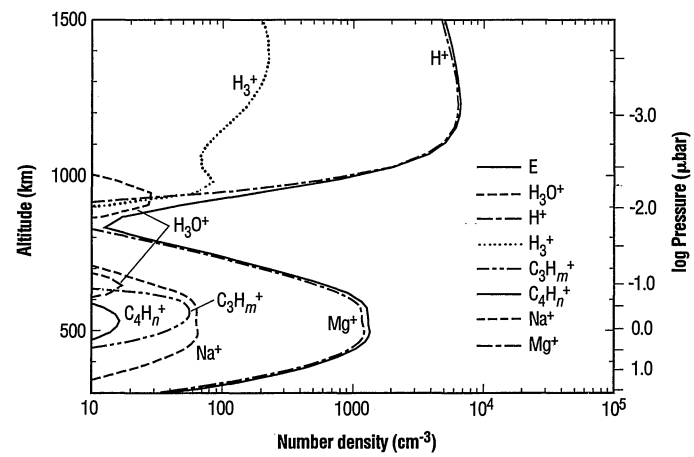

Fig. 4 (right). Model ion profiles for the lower ionosphere.

with the reaction $CH_5^+ + Mg \rightarrow Mg^+ + CH_4 + H$ (*24*). Because most of the metal species have high proton affinity (*25*), species such as MH^+ are also likely products. The large abundance of H ensures that MH^+ will be converted to M^+ by the reaction

$$MH^+ + H \rightarrow M^+ + H_2 \qquad (3)$$

analogous to the reaction $MO^+ + O \rightarrow M^+ + O_2$ in the terrestrial ionosphere (*26*). Theoretical estimates (*27*) of bond strengths in metal hydride ions shows that Eq. 3 will be exothermic for the metals considered here. In the model, charge exchange to form M^+ is assumed to form MH^+ with equal probability, and the rate for Eq. 3 is assumed to be 1×10^{-10} cm^3 s^{-1}. Because of reactions with CH_4, C_2 hydrocarbons, and water, Fe^+, S^+, and C^+ are not present in Fig. 4. Similar reactions with C_3 and larger hydrocarbons may occur for Mg^+ and Na^+, but apparently these have not been studied in the laboratory.

Clearly, the model lower ionosphere shown in Fig. 4 does not account for the observed electron layers. However, there is sufficient Mg^+ abundance predicted that the Mg^+ could be compressed into sharp layers. The short chemical lifetime of molecular ions makes them unsuitable as candidates for layer formation. According to the mechanism proposed to explain sporadic-E layers in the terrestrial ionosphere (*28*), compression of ions into layers can result from a horizontal wind with a vertical shear acting on the ions in the presence of a magnetic field. Such wind shears are usually produced by atmospheric gravity waves and tides.

The motions of ions and neutrals are coupled through ion-neutral collisions. However, in the presence of a magnetic field, ion motion is further influenced by the Lorentz force. By balancing the Lorentz force with the rate of momentum exchange due to collisions with neutrals, an algebraic expression may be derived (*29*) for the vertical ion velocity, w_i, in terms of the neutral wind components. The ratio of the ion-neutral collision frequency to ion gyro frequency, $\eta_i = \nu_{in}/\Omega_i$, characterizes the dominant influence on ion motion. At an altitude for which $\eta_i \gg 1$ (valid for $z < 800$ km) and, if we assume that the zonal wind u is the dominant neutral wind component, it can be shown (*29*) that $w_i \propto u/\eta_i$. Thus, changes in the horizontal wind are translated into changes in the vertical ion velocity.

Compression of the ions requires a convergent vertical ion wind, $\partial w_i/\partial z < 0$. Differentiating the equation for w_i with respect to z yields an expression relating the divergence of the vertical ion wind to the vertical shear in the zonal neutral wind (*29*). Figure 5 shows the result of applying an alternately convergent and divergent ion wind to the lower ionosphere shown in Fig. 4. [The lower ionosphere was first raised ~150 km, bringing the model profile into better agreement with the observations (*30*).] The prescribed wind was a sinusoid,

$$w_i = w_0 \sin [m (z - z_0)] \qquad (4)$$

where $m = 2\pi/d$ for a layer spacing $d \approx 33$ km, $z_0 = 633$ km, and $w_0 = 3$ ms^{-1}. This form of w_i results in the four layers seen in the lower portion of Fig. 5. The maximum vertical gradient of the ion wind is $\partial w_i/\partial z \approx 0.6$ m s^{-1} km^{-1}, which at an altitude of ~700 km corresponds (*29*) to a maximum $\partial u/\partial z \sim 30$ m s^{-1} km^{-1}, a substantial but not implausible wind shear.

The choice of a sinusoidal ion wind field was motivated both by the occurrence of multiple ion layers in the lower ionosphere and by the likelihood of vertically stratified zones of wind shear associated with atmospheric gravity waves. Earth-based stellar occultation data (*31*) of Neptune's upper atmosphere suggest the presence of convectively unstable waves at pressures as low as 0.1 to 0.03 μbar, with vertical wavelengths comparable to the ion layer spacing (~20 to 30 km) (*32*).

Laboratory data on the kinetics of neutral and ionized atomic metals, particularly Mg, in two-body, three-body, and cluster reactions with hydrocarbons and H_2 are crucial to a more complete understanding of the lower ionospheres of Neptune and the other giant planets. The detection (*33*) of abundant Mg and Mg^+ at the impact site of the G fragment of comet Shoemaker Levy 9 makes clear the need for further study of metals in reducing environments.

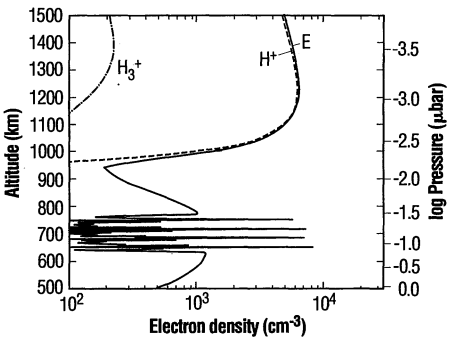

Fig. 5. Magnesium ions in the lower ionosphere are compressed into sharp layers by a sinusoidal vertical ion wind. The wind was applied from 630 to 770 km for a total of 5000 s, in steps of 500 s. The vertical resolution of the model has been enhanced to 2 km over this altitude range; elsewhere the resolution is one-third of a scale height. The lower ionosphere was first raised ~150 km by an upward ion wind of 1 m s^{-1}, applied from 400 to 1000 km for ~10^5 s. The upward wind is assumed to result from **E** × **B** drift and requires an electric field E of ~0.1 mV m^{-1}.

REFERENCES AND NOTES

1. E. C. Stone and E. D. Miner, *Science* **246**, 1417 (1989).
2. For a list of radio occultation publications before 1986, see (*6*). The ionosphere of Uranus is discussed in G. F. Lindal *et al.*, *J. Geophys. Res.* **92**, 14987 (1987); Neptune data are given in (*10*); Triton data are in (*8*). Note that G. F. Lindal is also known as G. Fjeldbo in earlier publications.
3. A review of the ionosphere of Venus is given by L. H. Brace and A. J. Kliore, *Space Sci. Rev.* **55**, 81 (1991). The ionosphere of Mars is discussed by C. A. Barth *et al.*, in *Mars*, H. Kieffer *et al.*, Eds. (Univ. of Arizona Press, Tucson, 1992), pp. 1054–1089.
4. M. C. Kelley, *The Earth's Ionosphere* (Academic Press, San Diego, 1989).
5. Plans are presently under way to use the existing array of Global Positioning System (GPS) satellites to study Earth's atmosphere and ionosphere by radio occultation (see G. A. Hajj, R. Ibañez-Meier, E. R. Kursinski, L. J. Romans, *Int. J. Imaging Syst. Technol.*, in press.
6. S. K. Atreya, *Atmospheres and Ionospheres of the Outer Planets and Their Satellites* (Springer-Verlag, Berlin, 1986).
7. R. H. Chen, *J. Geophys. Res.* **86**, 7792 (1981).
8. G. L. Tyler *et al.*, *Science* **246**, 1466 (1989).
9. G. Fjeldbo, V. R. Eshleman, O. K. Garriott, F. L. Smith III, *J. Geophys. Res.* **70**, 3701 (1965).
10. G. F. Lindal, *Astron. J.* **103**, 967 (1992).
11. In addition, it is possible that the signal variations were not fully resolved (*10*). The S-band spectra showed some broadening in the layer region; therefore, only X-band data were used for the approximately 20-s section of phase containing the sharp layers. These data were then converted to S band and merged with the remaining S-band data.
12. Sharp gradients in phase produce focusing and defocusing of rays and can, if the gradients are sharp enough or the spacecraft is far enough behind the planet, result in multipath propagation. The condition for multipath propagation is given by Fjeldbo *et al.* (*9*) in terms of the refractive gain,

$$G_r = -10 \log |1 + D d\alpha/d\rho|$$

where D is the distance from the limb to the spacecraft, α is the bending angle given by $\alpha = \lambda d\Delta\phi/d\rho$, and ρ is the height of the ray periapse relative to the center of the planet. At a caustic, rays cross, and in the geometric optics limit $G_r \rightarrow \infty$. Multipath propagation occurs when $D d\alpha/d\rho < -1$. From the phase variations (Fig. 1), it can be shown that this condition is not met at any time at either S or X band. However, the layers produce detectable defocusing of ~2 dB at S band and ~0.2 dB at X band.
13. J. E. P. Connerney, M. H. Acuna, N. F. Ness, *J. Geophys. Res.* **96**, 19023 (1991).
14. M. Allen *et al.*, *Ibid.* **86**, 3617 (1981).
15. J. I. Moses, *Icarus* **99**, 368 (1992).
16. E. K. Jessberger and J. Kissel, in *Comets in the Post-Halley Era*, R. L. Newburn *et al.*, Eds. (Kluwer Academic, Dordrecht, Netherlands, 1991), p. 1075.
17. P. N. Romani, J. Bishop, B. Bezard, S. Atreya, *Icarus* **106**, 442 (1994).
18. D. M. Hunten, R. P. Turco, O. B. Toon, *J. Atmos. Sci.* **37**, 1342 (1980).
19. R. C. Weast *et al.*, Eds., *CRC Handbook of Chemistry and Physics* (CRC Press, Boca Raton, FL, ed. 67, 1986), pp. F167–F177.
20. A. Canosa *et al.*, *J. Chem. Phys.* **97**, 1028 (1992).
21. J. E. P. Connerney and J. H. Waite, *Nature* **312**, 136 (1984).
22. D. F. Strobel, R. V. Yelle, D. E. Shemansky, S. K. Atreya, in *Uranus*, J. T. Bergstralh, E. D. Miner, M. S. Matthews, Eds. (Univ. of Arizona Press, Tucson, 1991), pp. 65–109.
23. Y. H. Kim and J. L. Fox, *Geophys. Res. Lett.* **18**, 123 (1991).
24. V. G. Anicich, *J. Phys. Chem. Ref. Data* **22**, 1469 (1993).
25. W. T. Huntress Jr., *Astrophys. J. Suppl. Ser.* **33**, 495 (1977).
26. E. E. Ferguson and F. C. Fehsenfeld, *J. Geophys. Res.* **73**, 6215 (1968).

27. G. Ohanessian and W. A. Goddard III, *Acc. Chem. Res.* **23**, 386 (1990); C. W. Bauschlicher Jr. and S. R. Langhoff, *Int. Rev. Phys. Chem.* **9**, 149 (1990).
28. J. D. Whitehead, *J. Atmos. Terr. Phys.* **20**, 49 (1961).
29. Following (*34*), balancing the Lorentz force and the rate of ion-neutral collisions gives $e\mathbf{v}_i \times \mathbf{B} = m_i\nu_{in}(\mathbf{v}_i - \mathbf{v}_n)$, where $\mathbf{v}_i$ and $\mathbf{v}_n$ are the ion and neutral velocity vectors. Solving for the vertical component of ion velocity yields $w_i = (u \cos I \cos D)/\eta_i$ for $u \gg v, w$, the meridional and vertical components of the neutral wind, and $\eta_i \gg 1$. Differentiating with respect to **z**,

$$\frac{\partial w_i}{\partial \mathbf{z}} = \cos I \cos D\left(\frac{\partial u}{\partial z} + \frac{u}{H_n}\right)\Big/\eta_i$$

where H_n is the scale height of the neutral atmosphere. The expressions $\nu_{in} = 2\pi(\alpha_{in}e^2/\mu_{in})^{1/2}n$ and $\Omega = eB/m_i$ are from (*6*).
30. The upward wind is usually attributed to $\mathbf{E} \times \mathbf{B}$ drift; in this case, the magnitude of the electric field (E) component perpendicular to B and z is $E_\perp \approx w_iB/\cos I = 0.1$ mV m^{-1}. Similar calculations have been made for Saturn's ionosphere [T. Majeed and J. C. McConnell, *Planet. Space Sci.* **39**, 1715 (1991)].
31. B. Sicardy, P. Goldreich, F. Roques, *Bull. Am. Astron. Soc.* **24**, 963 (1992); F. Roques *et al.*, *Astron. Astrophys.* **288**, 985 (1994).
32. A detailed discussion of gravity waves, including a time-dependent (propagating) wind field, will be present elsewhere (J. R. Lyons, in preparation).
33. K. Noll and the Hubble Space Telescope Team, *Int. Astron. Union Circ. 6038* (1994).
34. S. Kirkwood and P. N. Collis, *J. Atmos. Terr. Phys.* **51**, 259 (1989); W. A. Bristow and B. J. Watkins, *Geophys. Res. Lett.* **18**, 404 (1991).
35. Discussions with G. Lindal, E. R. Kursinski, J. Connerney, Y. Yung, W. Goddard, T. Rebold, and S. Asmar are gratefully acknowledged. G. Lindal provided the electron number density profile. This work was supported by NASA grants NAGW-2362 and NAGW-1509. Contribution 5418 from the Division of Geological and Planetary Sciences, California Institute of Technology.

29 July 1994; accepted 1 November 1994

Stress-Induced Vortex Line Helixing Avalanches in the Plastic Flow of a Smectic A Liquid Crystal

Richard A. Herke,* Noel A. Clark,† Mark A. Handschy

Dynamic surface force measurements of the response of a smectic A to layer normal stress exhibited time dependence for topological events in which single smectic layers were added or removed. Single layer–sized jumps in sample thickness had a rapid component of duration of ~1 second that produced most of the change in separation, but that was heralded by a slow precursor acceleration in separation, which began up to a few hundred seconds before. This avalanche-like dynamic signature is consistent with a relaxation mechanism based on the Glaberson-Clem-Bourdon instability of vortex lines (screw dislocations) in the smectic order parameter.

Smectic A's are liquid crystal phases having rod-shaped molecules organized into a one-dimensional (1D) stack of planar two-dimensional (2D) liquidlike layers, as shown in Fig. 1A. This hybrid 1D solid–2D liquid structure produces a variety of exotic elastic, hydrodynamic, and thermal effects (*1*). One of the most interesting of these is the phenomenon of oscillatory plastic flow, observed when the liquid crystal is confined between solid surfaces in a spherical wedge formed by the crossed cylinders of a surface force apparatus (SFA) (Fig. 1A). In response to the application of a constant rate of layer strain, the smectic A can exhibit oscillatory layer normal stress, apparently the result of events in which single molecular layers are either added or removed (*2–4*). These events are similar to those observed in isotropic liquids when confinement of the liquid between two closely spaced solid surfaces induces layering (*5*). We present here a study of the dynamics and mechanism of single layer jump events.

Condensed Matter Laboratory, Department of Physics, University of Colorado, Boulder, CO 80309, USA.

*Present address: Liquid Crystal Institute, Kent State University, Kent, OH 44242, USA.
†To whom correspondence should be addressed.

Such layering events are intrinsically topological in nature, which can be seen with the smectic A–superconductor–superfluid analogy of de Gennes (*1*, *6*) in which the smectic A layering is described by the two-component order parameter $\Psi(\mathbf{r}) = |\Psi(\mathbf{r})|e^{i\phi(\mathbf{r})}$. Here $|\Psi(\mathbf{r})|$ gives the local magnitude of the layering density wave, and the phase $\phi(\mathbf{r})$ advances by 2π on traversing a layer (where $\mathbf{r}$ is position). In the SFA, a constant $\phi(\mathbf{r})$ boundary condition is imposed on each solid surface so that changes in the layer number, for example, $n \rightarrow n - 1$ as in Fig. 1A, correspond to phase slippages of $\phi(\mathbf{r})$. Phase slippage with $\phi(\mathbf{r})$ fixed on the boundary must necessarily be mediated by vortex lines, the topological singularities of the field $\Psi(\mathbf{r})$. In the smectic A these are edge or screw dislocations (*7*). Although the nonuniform gap between the cylinders requires the presence of edge dislocations, our analysis indicates that in the macroscopic limit studied here (closest spacing of the cylinders, d_{min}, >2 μm), they are pinned and not involved in the layer jumps in a significant way.

This leaves screw dislocations to mediate the layering events, and the avalanche-like dynamic signature found in our experiments is consistent with a relaxation mechanism based on the Glaberson *et al.* (*8*)–Clem (*9*)–Bourdon *et al.* (*10*) helical instability of vortex lines found in $\Psi(\mathbf{r})$ systems. The helical instability of screwlike vortex lines was first discovered by Glaberson *et al.* while they were studying the effect of net fluid flow on quantized vortex lines in superfluid Helium II (*8*), and by Clem (*9*), who calculated the response to applied current of vortex flux lines in a type II superconductor. Bourdon *et al.* (*10*) showed that in a smectic A under either compressive or dilative strain, a previously straight screw dislocation line deforms into a helix to eliminate or add layers, respectively. Using the Oswald-Kléman analysis of this instability in the smectic A (*11*), we generated a computer simulation of the collective behavior of an array of screw dislocations under strain and found that a cascade of screw dislocation helixing instabilities did indeed reproduce the principal dynamic features that we observed.

As is typical in SFA studies, our sample, 4′-*n*-octyl-4-cyanobiphenyl (8CB) (*12*), was contained in a spherical wedge made from crossed molecularly smooth cylindrical surfaces of radius R and closest spacing d_{min}, with $d_{min} \ll R$. Layering jumps are observable for d_{min} as large as several microns in 8CB (*1*). We used a SFA of our design that enabled us to dynamically measure the force and surface separation (*13*). The cylindrical surfaces ($R = 1.2$ cm) were overlaid with thin pieces of mica (*2–5*), which were then coated with a monolayer of hexadecyltrimethylammonium bromide (HTAB) to provide a smooth surface that enforces homeotropic orientation (layers parallel to the surfaces). Motion of each of the surfaces was detected with a differential capacitance micrometer of sensitivity ~0.05 Å and an absolute accuracy ~10%. The position of the lower cylinder was servo controlled with a piezoelectric stack in conjunction with the capacitance micrometer. The upper cylinder was also attached to a spring of spring constant $K = 2.1 \times 10^7$ dynes/cm, which was mechanically in series with the effective spring of the liquid crystal layer between the cylinders, but which had a much smaller spring constant at low applied force. Displacement sensitivity was limited by electronic noise in the servo to ~ 0.02 Å over short time periods and by mechanical relaxation of ~0.2 Å/min over long periods. The time resolution of the SFA was intrinsically limited to ~0.03 s by the damping due to air flow in the capacitors and to ~0.4 s by analog-to-digital conversion. The SFA was contained in a temperature-controlled oven.

Data collection began with the placement of a drop of the smectic A 8CB in the gap between the cylinders. The surfaces